


Context-Specific Stress Causes Compartmentalized SARM1 Activation and Local Degeneration in Cortical Neurons

Flora I. Hinz,¹ Carmela Louise M. Villegas,¹ Jasmine T. Roberts,¹ Heming Yao,² Shreya Gaddam,² Anton Delwig,³ Samantha A. Green,⁴ Craig Fredrickson,¹ Max Adrian,⁵ Raymond R. Asuncion,⁶ Tommy K. Cheung,⁷ Margaret Hayne,¹  David H. Hackos,¹ Christopher M. Rose,⁷ David Richmond,² and Casper C. Hoogenraad¹

¹Department of Neuroscience, Genentech, Inc., South San Francisco, California 94080, ²Biological Research | AI Development, Genentech, Inc., South San Francisco, California 94080, and Departments of, ³Biochemical and Cellular Pharmacology, ⁴Discovery Chemistry, ⁵Pathology, ⁶Transgenic Technology, and ⁷Microchemistry, Proteomics, and Lipidomics, Genentech, Inc., South San Francisco, California 94080

Sterile alpha and TIR motif containing 1 (SARM1) is an inducible NADase that localizes to mitochondria throughout neurons and senses metabolic changes that occur after injury. Minimal proteomic changes are observed upon either SARM1 depletion or activation, suggesting that SARM1 does not exert broad effects on neuronal protein homeostasis. However, whether SARM1 activation occurs throughout the neuron in response to injury and cell stress remains largely unknown. Using a semiautomated imaging pipeline and a custom-built deep learning scoring algorithm, we studied degeneration in both mixed-sex mouse primary cortical neurons and male human-induced pluripotent stem cell-derived cortical neurons in response to a number of different stressors. We show that SARM1 activation is differentially restricted to specific neuronal compartments depending on the stressor. Cortical neurons undergo SARM1-dependent axon degeneration after mechanical transection, and SARM1 activation is limited to the axonal compartment distal to the injury site. However, global SARM1 activation following vacor treatment causes both cell body and axon degeneration. Context-specific stressors, such as microtubule dysfunction and mitochondrial stress, induce axonal SARM1 activation leading to SARM1-dependent axon degeneration and SARM1-independent cell body death. Our data reveal that compartment-specific SARM1-mediated death signaling is dependent on the type of injury and cellular stressor.

Key words: axon; cell death; neurodegeneration; SARM1

Significance Statement

Sterile alpha and TIR motif containing 1 (SARM1) is an important regulator of active axon degeneration after injury in the peripheral nervous system. Here we show that SARM1 can also be activated by a number of different cellular stressors in cortical neurons of the central nervous system. Loss or activation of SARM1 does not cause large-scale changes in global protein homeostasis. However, context-dependent SARM1 activation is localized to specific neuronal compartments and results in localized degeneration of axons. Understanding which cell stress pathways are responsible for driving the degeneration of distinct neuronal compartments under what cellular stress conditions and in which neuronal subtypes will inform the development of neurodegenerative disease therapeutics.

Introduction

Neuronal death occurs during both neurodevelopment and neurodegenerative diseases. Dysregulation of the neuronal death

processes may lead to various neurological disorders and, depending on the neuronal population affected, specific aphasias, dementias, or motor disorders. Surprisingly, recent studies have shown that axonal degeneration and cell body death, which together underlie neuronal death, appear to be separate and active processes that may be regulated independently in response to different types of stressors and the localization of those stress signals (Pemberton et al., 2021). It is currently unclear whether these processes occur in parallel or sequentially during disease progression, whether inhibiting one may delay the other, and whether this has implications for future therapeutic development (Dadon-Nachum et al., 2011).

While we are still far from understanding how and in what contexts cell bodies and axons execute their own disassembly,

Received Dec. 26, 2023; revised April 21, 2024; accepted April 23, 2024.

Author contributions: F.I.H. and C.C.H. designed research; F.I.H., C.L.M.V., J.T.R., A.D., C.F., R.R.A., T.K.C., and M.H. performed research; H.Y., S.G., S.A.G., M.A., D.H.H., and D.R. contributed unpublished reagents/analytic tools; F.I.H., T.K.C., and C.M.R. analyzed data; F.I.H. and C.C.H. wrote the paper.

We thank Tiffany Heaster-Ford for helping optimize the SARM1 activation imaging. We thank Steve Vito for the use and advice on primary antibodies used for immunocytochemistry experiments and members of the Hoogenraad Lab for their helpful suggestions during the study.

The authors declare no competing financial interests.

Correspondence should be addressed to Casper C. Hoogenraad at hoogenraad.casper@gene.com.

<https://doi.org/10.1523/JNEUROSCI.2424-23.2024>

Copyright © 2024 the authors

critical components of these pathways have been identified in the last decade. Specifically, anti- and proapoptotic B-cell lymphoma-2 protein family members are now widely recognized to play key roles in the regulation of neuronal cell body death (Moujalled et al., 2021). Furthermore, mitogen-activated protein kinase signaling pathways, among them the dual leucine zipper kinase (DLK) stress-response pathway, have been shown to play key roles in neuronal cell death during development and neurodegeneration (Kim and Choi, 2015). Activation of DLK induces stress-specific JNK signaling and generates a broad transcriptional response in neurons through the regulation of transcription factors, such as c-Jun, which leads to apoptosis (Farley and Watkins, 2018; Siu et al., 2018; Jin and Zheng, 2019).

More recently, the central role of sterile alpha and TIR motif containing 1 (SARM1) and its regulation by nicotinamide nucleotide adenyltransferase 2 (NMNAT2) in injury-induced axon degeneration of peripheral neurons, an active process also known as Wallerian degeneration, has been identified (Coleman and Höke, 2020; Loring and Thompson, 2020). SARM1 is an autoinhibited NADase (Gerdts et al., 2015; Essuman et al., 2017; Loring et al., 2020; Sporny et al., 2020), which acts as a metabolic sensor (Figley et al., 2021). It can be activated by an endogenous change in the relative concentrations of nicotinamide mononucleotide (NMN) to nicotinamide adenine dinucleotide (NAD^+) which in axons is regulated by NMNAT2 or exogenously by metabolic derivatives of the rodenticide vacor (Loreto et al., 2021). Work from a number of labs over the last years has shown that in dorsal root ganglion (DRG) sensory neurons of the peripheral nervous system, SARM1 activation leads to dramatic loss of NAD^+ and ATP levels, mitochondrial membrane potential loss, calcium influx, and subsequent calpain activation and morphological axon dissociation (Coleman and Höke, 2020; Ko et al., 2021). SARM1, via the N-terminal 25 amino acids, is localized to the outer mitochondrial membrane (Panneerselvam et al., 2012; Gerdts et al., 2013; Miyamoto et al., 2024) and is present on mitochondria throughout both the neuronal cell body and axon. It remains unclear which types of cellular stress result in SARM1-dependent neurodegeneration, whether this is neuronal cell type dependent, whether SARM1 activation occurs in a localized manner in response to these stressors, and whether that results in localized axon degeneration, cell body death, or both.

In this study, we show that SARM1 activation is restricted to specific neuronal compartments depending on the stressor. Using the fluorescent SARM1 activity probe, AD-1a (K. Huang et al., 2023), we demonstrate that SARM1 is activated by a variety of cell stress mechanisms, including injury and microtubule and mitochondrial dysfunction in cortical neurons. While SARM1 activation occurs throughout the cell body and axon in response to global SARM1 activation by vacor and results in both SARM1-dependent cell body death and axon degeneration, mechanical injury and microtubule dysregulation result in SARM1 activation specifically in the axonal compartment. SARM1 inhibition can delay axon degeneration caused by these stressors but has little effect on cell body death. Furthermore, we confirm that SARM1 in cortical neurons exerts its function by reducing NAD^+ levels and does not alter global protein homeostasis. Taken together, we found that SARM1 activation is localized to distinct subcellular compartments in response to specific stressors and plays a crucial role in axon degeneration in neurons of the central nervous system.

Materials and Methods

Reagents

Vincristine (V8879), taxol (T7191), rotenone (CRM38703), NAD^+ (10127965001), and nicotinamide (N0636) were purchased from Sigma-Aldrich. CZ-48 (HY-129522) was purchased from MedChemExpress. 8-Br-cADPR (18442) was purchased from Cayman Chemical. AD-1a was synthesized as described in K. Huang et al. (2023).

Synthesis of vacor

A 250 ml round-bottom flask equipped with a stir bar was charged with 4-nitrophenyl isocyanate (15.33 g, 1 equiv, 93 mmol) and diluted with dichloromethane (120 ml). The reaction was cooled to 0°C using an ice-water bath, after which 3-(aminomethyl)pyridine (10 g, 1 equiv, 93 mmol) was added slowly to the reaction (caution, exotherm). The reaction was warmed to room temperature at which point a light-yellow product started precipitating. The reaction was stirred overnight at room temperature. The solid was filtered and further dried under high vac to yield vacor as a light-yellow solid (23 g, 91% yield):

LCMS: (ESI, m/z) $[\text{M} + \text{H}]^+ = 273.0$

^1H NMR (400 MHz, DMSO) δ 9.44 (s, 1H), 8.54 (d, $J = 2.2$ Hz, 1H), 8.46 (dd, $J = 4.8, 1.6$ Hz, 1H), 8.18–8.10 (m, 2H), 7.72 (dt, $J = 7.9, 2.0$ Hz, 1H), 7.68–7.60 (m, 2H), 7.36 (ddd, $J = 7.8, 4.8, 0.8$ Hz, 1H), 7.02 (t, $J = 6.0$ Hz, 1H), 4.35 (d, $J = 5.9$ Hz, 2H)

Animals

Transient receptor potential cation channel, subfamily M, member 2 (TRPM2) KO mice were generated by Genentech as described in Tang et al. (2010). $B6.129 \times 1\text{-Sarm1tm1Aidi/J}$ (RRID:IMSR_JAX:018069) was obtained from The Jackson Laboratory. The $B6.129 \times 1\text{-Sarm1tm1Aidi/J}$ mice were generated so that *Sarm1* exons 3–6 were replaced with a neomycin resistance gene in reverse orientation (Kim et al., 2007). To generate experimental mice (SARM1 wt/wt; neoR neg and SARM1 ko/ko; neoR pos), we bred SARM1 mice as an in-house colony. Each mouse had tail snips genotyped in-house to detect SARM1 and the neomycin cassette.

To prepare primary embryonic cortical cultures, we obtained both male and female embryos from timed pregnant C57BL/6N mice from Charles River Laboratories as well as timed pregnant SARM1 wt/wt; neoR neg mice and SARM1 ko/ko; and neoR pos mice, TRPM2 wt/wt mice, and TRPM2 ko/ko mice. Mice were housed on a regular light/dark cycle (14:10 h) with *ad libitum* access to food (LabDiet 5010) and water. All animal care/handling procedures were reviewed and approved by Genentech's Institutional Animal Care and Use Committee and were conducted in full compliance with regulatory statutes, Institutional Animal Care and Use Committee policies, and National Institutes of Health guidelines.

Dissociated primary mouse cortical neuron cultures

Cortices from both male and female Day 15 embryos (E15) were dissected, stripped of meninges, washed 3 \times with cold HBSS (Invitrogen, 14170-112), and incubated for 10 min at 37°C in HBSS supplemented with 0.25% trypsin (Invitrogen, 15090-046) and DNase I (Roche Holding, 104159). The tissue was washed 3 \times with HBSS and triturated in plating media containing DNase I [Neurobasal medium (Thermo Fisher Scientific, 21103-049), 20% heat-inactivated horse serum (Thermo Fisher Scientific, 26050-088), 25 mM sucrose, and 0.25% Invitrogen GlutaMAX (Thermo Fisher Scientific, 35050-061)]. Dissociated cells were centrifuged at 125 g for 5 min at 4°C, resuspended in a plating medium, and plated in poly-L-lysine-coated (MilliporeSigma, P1274) plates. After 24 h, the plating medium was replaced with NBActiv4 (BrainBits, NB4500). Cells were maintained at 37°C with 5% CO_2 , and the medium was renewed using 50% exchange every 3–4 d.

For "spot cultures" used for axon degeneration assays and axon imaging, ~40,000 cells in a volume of 1.25 μl were plated on the center of a 48-well plate and incubated at 37°C with 5% CO_2 for 20 min, after which the well was flooded with plating media. For cytotoxicity dye uptake and biochemical assays, cells were plated in 96-well plates at a density of 30,000 cells per well. For scratch wound assays, cells were plated in Incucyte ImageLock plates at a density of 50,000 cells per well. For

proteomics experiments, cells were plated in 10 cm tissue culture plates at a cell density of five million cells per plate. All experiments were performed between DIV7–10.

Dissociated primary mouse microglia and astrocyte cultures

Microglia and astrocytes were isolated from both male and female mouse pups between 1 and 3 d old as described in Byrnes et al. (2024). Briefly, cortices were isolated, and meninges were removed; the tissue was washed in cold HBSS (Invitrogen, 14170-112), then trypsinized (Invitrogen, 15090-046), and filtered through 70 μm filters. Homogenate was incubated in DMEM media supplemented with GlutaMAX (Thermo Fisher Scientific, 35050-061) and 10% fetal bovine serum. Microglia were shaken off after 10–14 d of culture when cells were observed to be floating freely, and astrocytes were then shaken overnight to remove any remaining microglia and trypsinized and replated the following day. Both microglia and astrocytes were plated at 250,000 cells/ml.

Human iPSC-derived cortical cultures

The human-induced pluripotent stem cell (hiPSC) line, iP11N (male), stably expressing a doxycycline-inducible Neurogenin-2 (NGN2) cassette (ALSTEM, catalog #iP11N), was used for all differentiations. The NGN2-iNeuron differentiation and maturation were performed following the protocol previously published (Shan et al., submitted) with some modifications. In brief, hiPSCs were maintained in mTeSR Plus media (100-0276; STEMCELL Technologies) using the substrate iMatrix-511 (NP892-01; REPROCELL). When iPSC cultures reached ~75% confluency, they were passaged using ReLeSR (100-0483; STEMCELL Technologies). Cultures underwent a minimum of three passages after thawing before initiating differentiations. On Day 0, ~75% confluent iPSC cultures were dissociated into single cells using Accutase (07920; STEMCELL Technologies) and seeded at a density of 40,000 cells/cm² on iMatrix-511 substrate in induction media [DMEM/F-12 (2133-020; Thermo Fisher Scientific), B27, N-2 Max (AR009; R&D Systems), GlutaMAX (35050061; Thermo Fisher Scientific), NEAA, 10 μM SB431542, 2 μM XAV939, 10 μM DAPT, 100 ng/ml Noggin] containing Y27632 (S1049; Selleck Chemicals). Neural induction was achieved by supplementing induction media with 3 $\mu\text{g}/\text{ml}$ doxycycline and performing daily media changes for 5 consecutive days. On Day 5, the media was changed to maturation media [Neurobasal medium (21103-049; Thermo Fisher Scientific), B27, GlutaMAX (35050061; Thermo Fisher Scientific), 20 ng/ml BDNF, 20 ng/ml GDNF, 1 ng/ml TGF β 3, 500 μM cAMP, 10 μM DAPT] with doxycycline concentrations reduced to 2 $\mu\text{g}/\text{ml}$. Maturation media were also supplemented with cytosine β -D-arabinofuranoside hydrochloride (Ara-C, C6645-100MG; Sigma-Aldrich) at 5 μM (to eliminate any remaining dividing cells) and left in the culture medium for 2 d. On Day 7, cultures were treated with Accutase for 20 min followed by the addition of maturation media containing deoxyribonuclease I (LK003172; Worthington Biochemical). Cultures were gently triturated using a serological pipette, passed through a 40 μm cell strainer, and centrifuged. After resuspension in CryoStor (100-1061; STEMCELL Technologies) cryopreservation media, banks of Day 7 induced NGN2 (iNGN2) neurons were created. Day 7 iNGN2 neurons were then thawed and seeded in maturation media supplemented with 2 $\mu\text{g}/\text{ml}$ doxycycline on poly-D-lysine (P7280; Sigma-Aldrich) and iMatrix-511-coated tissue culture plates. At the time of seeding, “spot cultures” were achieved by resuspending 50,000 cells into a 2 μl droplet and localizing it to the center of each well of a dry, substrate-treated 48-well plate. The iNGN2 iNeurons in the droplets were incubated and allowed to attach for 20 min, at which time the wells were slowly flooded with maturation media. Doxycycline treatment was continued for the next 7 d with one-third of media exchanges being performed three times per week. Following the 7 d doxycycline treatment, one-third of media exchanges, using maturation media, were performed three times per week for 2 weeks (28 d in culture).

Axon degeneration assays

Spot culture axon injury was performed manually under a dissection microscope using a crescent blade microknife (Fine Science Tools).

Axon stress treatment and SARM1 inhibitor addition were performed as part of a 50% media change.

Immediately after treatment or injury, plates were placed into an Incucyte Live-Cell Analysis System, and phase contrast images were automatically captured every 2 h for 72–96 h. Two images per well were selected and exported for analysis.

For the scratch wound assay, the scratch was made using the Incucyte Wound Maker 96 Tool. Subsequently, the cells were imaged and scratch area detected using the Incucyte Live-Cell Analysis System over a 72 h period.

Development of an automated algorithm for quantification of axon degeneration

Algorithm design. We developed an automatic scoring algorithm based on two convolutional neural networks: a unary model and a transition model. The unary model takes as input a single image containing a field of axons and outputs a probability for each of the four possible degeneration scores (Extended Data Figure 1-2a). The transition model takes as input a pair of images from the same field of neurons at consecutive time points and predicts the probability of the score change between the two images (Extended Data Figure 1-2b). Both the unary and transition models leverage an EfficientNet-B0 backbone that was pretrained on ImageNet. Finally, the unary and transition models are combined as shown in Extended Data Figure 1-2c, where gray boxes represent the predicted score probabilities for each individual image from the unary model and arrows represent the predicted score transition probabilities for a pair of consecutive images from the transition model. Given the predicted probabilities from the unary and transition models, we infer a globally optimal score sequence (shown in cyan) using dynamic programming (Viterbi algorithm).

Algorithm training. The unary model and transition model were both trained on 33,990 manually scored images from 61 axon degeneration time-lapse experiments (images were collected every 2 h for 72 h). The models were trained to minimize cross-entropy between the algorithm prediction and the manually annotated ground truth, using the Adam optimizer, a learning rate of 0.0001, and a batch size of 16. Data augmentation, including random rotation, random crop, random horizontal, and vertical flips, was applied to increase the diversity of the training images and thereby improve the model's invariance to confounders.

Performance evaluation. The performance of the algorithm was evaluated on a test set containing 7,399 scored images from 13 held-out experiments. Experiments were held out based on timestamp (most recent experiments were used for testing), to create a challenging test set that is representative of real-world deployment. The algorithm achieves an overall accuracy of 80% on the held-out test set.

Due to the subjective nature of the annotation process, we also collected a multiannotator test set, consisting of 1,477 images from 17 experiments independently scored by two annotators. We compared the agreement between the algorithm's predictions and the scores from the two annotators and found that the algorithm achieves the same inter-rater variability as the human annotators (Extended Data Figure 1-3). Thus, the algorithm is interchangeable with the manual annotation process. See Extended Data Figure 1-3c for representative examples of time-lapse scoring curves from two human annotators and our algorithm.

Fluorescent and luminescence assays

NAD⁺ and ATP levels were measured using the Promega NAD/NADH-Glo (G9072) and CellTiter-Glo (G7572) kits following manufacturer's recommendations, respectively. Dead cell puncta were measured by adding IncuCyte Cytotox Red Reagent (4632) to the cell culture medium at a final dilution of 1:4,000, capturing both phase and red fluorescence images using the IncuCyte Live-Cell Analysis System every 2 h over a period of 72 h and quantifying red puncta using the built-in analysis modules. The mitochondrial membrane potential was measured using the Image-iT TMRM Reagent (Invitrogen, 134361) according to the manufacturer's instruction and imaged using the IncuCyte Live-Cell Analysis System. To measure neurofilament light (NFL) levels released by cortical neurons into the media, we used the supernatant

from neurons in NF-L ELISA (UmanDiagnostics, 10-7002) according to the manufacturer's instructions.

AD-1a fluorescence imaging

A Rigaku Wizard pH buffer block (Rigaku, catalog #1008654) was used to test the effect of pH on 1a fluorescence. This kit contains 96 buffers spanning a pH range from 2.4 to 11.6. The stock buffers were first diluted 1:10 in water. Then 1a was mixed with each of these buffers at a final concentration of 10 μ M. Fluorescence (in arbitrary fluorescence units) was measured using the M1000 plate reader (Tecan Trading) with excitation at 445 nm and emission detection at 595 nm.

Spot cultures were treated with stressors and 1a (25 μ M final concentration) as part of a 50% media change. Confocal images were acquired on a 3i Marianas spinning disk confocal microscope (Intelligent Imaging Innovations), built on a Axio Observer with 20 \times Plan Apo 0.8 NA, 40 \times Plan Apo 1.4 NA, and 63 \times Plan Apo 1.4 NA objectives (Carl Zeiss) and a CSU-W 50 μ m spinning disk (Yokogawa Electric). In addition, the microscope is equipped with a Mesa Light homogenizer and four-line LaserStack (Intelligent Imaging Innovations), Definite Focus 2 (Carl Zeiss), a stage-top incubator (Okolab), and Prime95B cMOS cameras (Photometrics). Data acquisition was done through the SlideBook 6 software (Intelligent Imaging Innovations). To acquire AD-1a signal, we used 488 nm excitation and collected emission light with a 620–40 nm filter (Semrock). Images were analyzed using ImageJ2 (2.3.0).

Proteomic sample preparation

Five hundred microgram of protein lysate in denaturing buffer (8 M urea, 20 mM HEPES, pH 8.0) was reduced [5 mM dithiothreitol (DTT), 45 min at 37°C], alkylated (15 mM iodoacetamide, 20 min at room temperature in the dark), and quenched (5 mM DTT, 15 min at room temperature in the dark). Proteins were pelleted by chloroform–methanol precipitation. The resulting pellet was resuspended in a denaturing buffer, diluted to 4 M urea, and digested for 4 h at 37°C with lysyl endopeptidase (FUJIFILM Wako Chemicals) at an enzyme:protein ratio of 1:100. The sample was further diluted to 1.3 M urea and subjected to overnight enzymatic digestion at 37°C with sequencing grade trypsin (Promega; enzyme:protein ratio, 1:50). Resultant peptides were acidified with 20% trifluoroacetic acid (TFA, 1% final concentration), centrifuged at 18,000 \times g for 15 min, and desalted using a Sep-Pak C18 column (Waters).

For global proteome samples, 100 μ g of peptides from each sample was dissolved in 100 mM HEPES, pH 8.0 (1 mg/ml). Isobaric labeling was performed using TMTpro16-plex reagents (Thermo Fisher Scientific). Each unit (0.5 mg) of TMT reagent was allowed to reach room temperature immediately before use, spun down on a benchtop centrifuge, and resuspended with occasional vortexing in 20 μ l anhydrous acetonitrile (ACN) prior to mixing with peptides (18% final ACN concentration). After incubation at room temperature for 1 h, the reaction was quenched for 15 min with 20 μ l of 5% hydroxylamine. Labeled peptides were combined in equimolar ratios and dried. The TMTpro-labeled sample was redissolved in 80 μ l 0.1% TFA and centrifuged at 16,000 \times g, and the supernatant was processed further. Off-line high-pH reversed-phase fractionation was performed on a 1100 HPLC system (Agilent) using an ammonium formate-based buffer system. Peptides (400 μ g) were loaded onto a 2.1 \times 150 mm 3.5 μ m 300 Extend-C18 Zorbax column (Agilent) and separated over a 75 min gradient from 5 to 85% ACN into 96 fractions (flowrate, 200 μ l/min). The fractions were concatenated into 24 fractions, mixing different parts of the gradient to produce samples that would be orthogonal to downstream low-pH reversed-phase liquid chromatography–tandem mass spectrometry (LC–MS/MS). Fractions were dried and desalted using C18 stage tips as previously described (Rappsilber et al., 2007). Peptides were lyophilized and resuspended in 10 μ l buffer A (2% ACN, 0.1% formic acid) for LC–MS/MS analysis.

MS analysis

For global proteome, LC–MS/MS analysis was performed by injecting \sim 1 μ g (proteome) of each fraction on an Orbitrap Eclipse mass spectrometer (Thermo Fisher Scientific) coupled to a Dionex Ultimate 3000 RSLC (Thermo Fisher Scientific) employing a 25 cm IonOpticks Aurora series column (IonOpticks) with a gradient of 2–30% Buffer B (98% ACN; 2% H₂O with 0.1% FA; flow rate, 300 nl/min). Global

proteome samples were analyzed with a total run time of 95 min. The samples on Orbitrap Eclipse were collected with FTMS1 scans at 120,000 resolution with an AGC target of 1×10^6 and a maximum injection time of 50 ms. FTMS2 scans on precursors with charge states of 3–6 were collected at 15,000 resolution with collision-induced dissociation fragmentation at a normalized collision energy of 30%, an AGC target of 2×10^4 , and a max injection time of 100 ms (proteome).

Real-time database search (RTS) was performed prior to acquisition of MS3 spectra using the InSeqAPI software (Budayeva et al., preprint), which operated similarly to previously published approaches (Erickson et al., 2019; Schweppe et al., 2020). The following RTS parameters were used for global proteome analysis: UniProt human database August 2021 version, including 218,136 Swiss-Prot sequences of canonical and protein isoforms, plus common contaminants and decoys; static modifications including Cys carbamidomethylation (+57.0215), Lys, and n-term TMTpro (+304.207146); and variable modifications including Met oxidation (+15.9949) and Tyr TMTpro (+304.207146). Off-line search was performed using comet v.2019.01 with parameters matched to the RTS search. Peptide false discovery rate was filtered to <1% using a linear discriminant algorithm. TMT reporter ions produced by the TMT tags were quantified with the Mojave in-house software package by calculating the highest peak within 20 ppm of theoretical reporter mass windows and correcting for isotope purities.

Quantification and statistical testing of global proteome proteomics data were performed by the MSstatsTMT_2.0.1 R package (T. Huang et al., 2020) Multiple fractions from the same TMT mixture were combined in MSstatsTMT v2.0.1 (T. Huang et al., 2020). In particular, if the same peptide ion was identified in multiple fractions, only the single fraction with the highest maximal reporter ion intensity was kept. Global median normalization was carried out to reduce the systematic bias between channels.

Raw proteomics data are publicly available within MassIVE (a member of the ProteomeXchange consortium) and can be found with the identifier MSV000093524.

Immunoblot

Cortical, astrocyte, and microglial cultures were washed in PBS, dissociated in 0.25% prewarmed trypsin, washed in PBS, and pelleted by centrifugation at 5,000 \times g for 1 min at room temperature. Cell pellets were resuspended in 40–50 μ l TNT buffer (150 mM NaCl, 1 mM EDTA, 50 mM Tris, pH 7.4, 1% Triton X-100) supplemented with protease and phosphatase inhibitors (Roche Holding, 4693159001 and 4906845001). Lysates were incubated at 4°C for 30 min with constant agitation and centrifuged at 13,000 \times g for 5 min at 4°C. The supernatant was transferred to a new tube, and equal volumes of Laemmli sample buffer (Bio-Rad Laboratories, 161-0737) supplemented with β -mercaptoethanol were added to the lysate. Lysates were briefly heated to 95°C, loaded onto NuPAGE 4–12% Bis-Tris Midi Gels (Invitrogen, WG1403BOX), and run at 140 V for \sim 1.5 h. Samples were transferred to nitrocellulose membranes (Bio-Rad Laboratories, 1704159), blocked with 3% BSA in PBST for 1 h at room temperature, probed with primary antibody overnight at 4°C, washed with PBS with Tween 20 (PBST), and probed with secondary antibody for 1 h at room temperature. Primary antibodies used are as follows: ring finger protein 167 (RNF167; 1:1000; Invitrogen, PA5-103821), SARM1 (1:1000; Invitrogen, MA5-42379), IBA1 (1:1000; FUJIFILM Wako Chemicals, 019-1974), GFAP (1:1000; Invitrogen, 13-0300), β -III-tubulin (1:1000; Abcam, ab18207), and β -actin (1:2000; Sigma-Aldrich, A1978).

Immunocytochemistry

Cortical cultures were fixed in 4% PFA, washed in PBS, blocked in 5% normal donkey serum (Jackson ImmunoResearch, 017-000-121) +0.1% Triton X-100 in PBS (blocking buffer), and probed with primary antibodies in blocking buffer overnight at 4°C. Subsequently, cultures were washed in PBS, probed with secondary antibodies in 5% normal donkey serum in PBS for 1 h at room temperature, washed in PBS, and incubated with Hoechst 33342 (BD PharMingen, 561906) for 20 min at room temperature. Confocal images were acquired on a 3i Marianas spinning disk confocal microscope (Intelligent Imaging Innovations), built on a Axio Observer with a 63 \times Plan Apo 1.4 NA objective (Carl Zeiss) and a

CSU-W 50 μm spinning disk (Yokogawa Electric). Primary antibodies used are as follows: NeuN (1:1000; EMD Millipore, ABN90) and GFAP (1:500; Invitrogen, 13-0300).

Statistical analysis

Data plotting and statistical analyses were performed using Prism 9.5.1 (GraphPad Software).

Results are presented as mean \pm SEM, and all experiments were completed at least in biological triplicate, unless otherwise noted. Statistical tests used are noted in the figure legends and in Extended Data Table 1-1. Unless otherwise noted, statistical significance was defined as $p < 0.05$.

Results

Cortical neurons undergo SARM1-dependent axon degeneration after injury

To study the role of SARM1 in axon degeneration of cortical neurons, we adapted a spot plating procedure previously developed for DRG cultures (Miller et al., 2009; Gerdts et al., 2015; Avraham et al., 2022) in which $\sim 40,000$ dissociated embryonic mouse cortical neurons from either WT or SARM1 KO mice are plated onto a small, central area of a 48-well plate. These cells are allowed to attach to the plate before the wells are flooded with media. Over the next 7–9 d, the cell bodies remain in their original location, while both dendrites and axons grow outward, enabling mechanical separation of the cell bodies and neurites (Fig. 1*a*). As dendrites only grow a few tens of micrometers, the neuronal transections that are made $\sim 50 \mu\text{m}$ from the edge of the cell body field affect mainly axons. The axon field distal to the injury is monitored continually using phase imaging over the next 72 h. While axons of WT cortical neurons degenerate within 12 h of injury, blebbing, and then fragmenting, SARM1 KO neurons remain morphologically intact for over 72 h (Fig. 1*b*).

To quantify axon degeneration, we scored the resulting images on a scale of 1–4, where a score of 1 denotes completely healthy, continuous axons, a score of 4 denotes completely degenerated and fragmented axons, and scores of 2 and 3 represent intermediate stages of degeneration (Extended Data Figure 1-1). Using this manually annotated data set, we developed a custom deep learning algorithm for scoring axon degeneration in time-lapse microscopy images (see Materials and Methods, Algorithm training, for detailed description; Extended Data Figures 1-2–1-3). The algorithm is deployed in a high-performance computing environment and automatically scores axon degeneration experiments within a few hours without the need to crop images to exclude sites of injury or cell bodies. It was used to score all phase microscopy images of axon degeneration in this study. Using this combination of spot cultures, automatic imaging, and AI-assisted scoring of morphological axon degeneration, our platform is capable of quantifying axon degeneration in a semihigh-throughput manner.

As previously described for neurons of the peripheral nervous system (Gerdts et al., 2013, 2015), the loss of SARM1 resulted in almost complete absence of morphological signs of axon degeneration in response to injury for over 72 h (Fig. 1*c*). The addition of a SARM1 small-molecule inhibitor to the media at the time of injury in WT neurons resulted in axon protection after injury for over 48 h (Fig. 1*d*). Similarly, SARM1 inhibition almost completely abolished axon degeneration in response to axonal injury in human iPSC-derived cortical neurons over a period of 72 h (Fig. 1*e*). Taken together, we find that similar to mouse sensory DRG neurons, both mouse and human cortical neurons undergo SARM1-dependent axon degeneration in response to mechanical injury.

Neurite outgrowth is not affected by the loss of SARM1

While the importance of SARM1 as the central executioner of axon degeneration has been well established (Coleman and Höke, 2020), the physiological benefit of active SARM1-mediated axon degeneration in response to injury still remains unclear. One hypothesis proposes that active axon degeneration enables more rapid outgrowth of new axons after injury (Shin et al., 2014) and SARM1, like DLK (Tedeschi and Bradke, 2013), may also be involved in regulating axon outgrowth after injury. To test this hypothesis, we used dissociated mouse cortical cultures seeded in a 96-well format. Cells were injured using a pin tool, and neurite regrowth into the injury site was monitored over time. Using this approach, we could not detect a significant difference in neurite outgrowth between WT and SARM1 KO neurons (Fig. 1*f,g*). Furthermore, the inhibition of neurite outgrowth using low concentrations of the microtubule stabilizer taxol resulted in a similar delay, suggesting that neurite outgrowth mechanisms do not differ between WT and SARM1 KO neurons. Therefore, while SARM1 plays a clear role in axon degeneration after injury in mouse cortical neurons, we find no evidence that SARM1 plays a role in neurite outgrowth in this cell type.

SARM1 activation is localized to the axonal compartment distal of the injury site

SARM1 is a NAD^+ -consuming enzyme that catalyzes the exchange of nicotinamide (NAM) moiety with water or its own adenine moiety to form ADP-ribose (ADPR) or cyclic ADPR (cADPR), respectively (Gerdts et al., 2015; Essuman et al., 2017). However, in the presence of other basic heterocycles, SARM1 can catalyze a base-exchange reaction to form NAM-substituted synthetic NAD^+ analogs (Hughes et al., 2021; Bratkowski et al., 2022). Huang and colleagues utilized this mechanism to develop fluorescent probes such as PC6 and AD-1a to monitor SARM1 activity (W. H. Li et al., 2021; K. Huang et al., 2023). When the cell membrane-permeable compound 1a is added to live cells with active SARM1, it is converted by SARM1 into a membrane-impermeable fluorescent molecule, AD-1a, which accumulates in the cells (Fig. 2*a*). While this base-exchange reaction is specifically catalyzed by SARM1 (Angeletti et al., 2022; K. Huang et al., 2023), we found that even in SARM1 KO neurons, we could detect background signals, reminiscent of cellular vesicles. As the large spectral shift and concomitant gain in fluorescence of the 1a probe is driven by the SARM1-catalyzed addition of a positive charge that delocalizes over the conjugated π -system of AD-1a, we hypothesized that the fluorescence of 1a may be directly modulated by its ionization state. To investigate this ionization-dependent behavior, the fluorescence of 1a was measured across a wide range of pH values (Fig. 2*b*). The fluorescence of 1a displayed a clear pH dependence, with increases of up to 1,000-fold under lower pH conditions. Notably, the fluorescence of 1a at pH levels below 5 was similar to that of AD-1a in SARM1-catalyzed biochemical reactions. Therefore, the SARM1-independent background signals likely result from 1a uptake into low-pH vesicles, such as lysosomes and endosomes, which have pH values as low as 4.5 (Casey et al., 2010).

SARM1 activity can be measured by the loss of NAD^+ or production of ADPR and cADPR (Sasaki et al., 2020). Detection of these metabolites relies on biochemical endpoint assays such as NAD/NADH-Glo or LC-MS, which do not allow easy investigation of the kinetics and subcellular localization of SARM1 activation. Utilizing the newly developed fluorescent probe AD-1a, we show that AD-1a fluorescence increases in WT mouse cortical

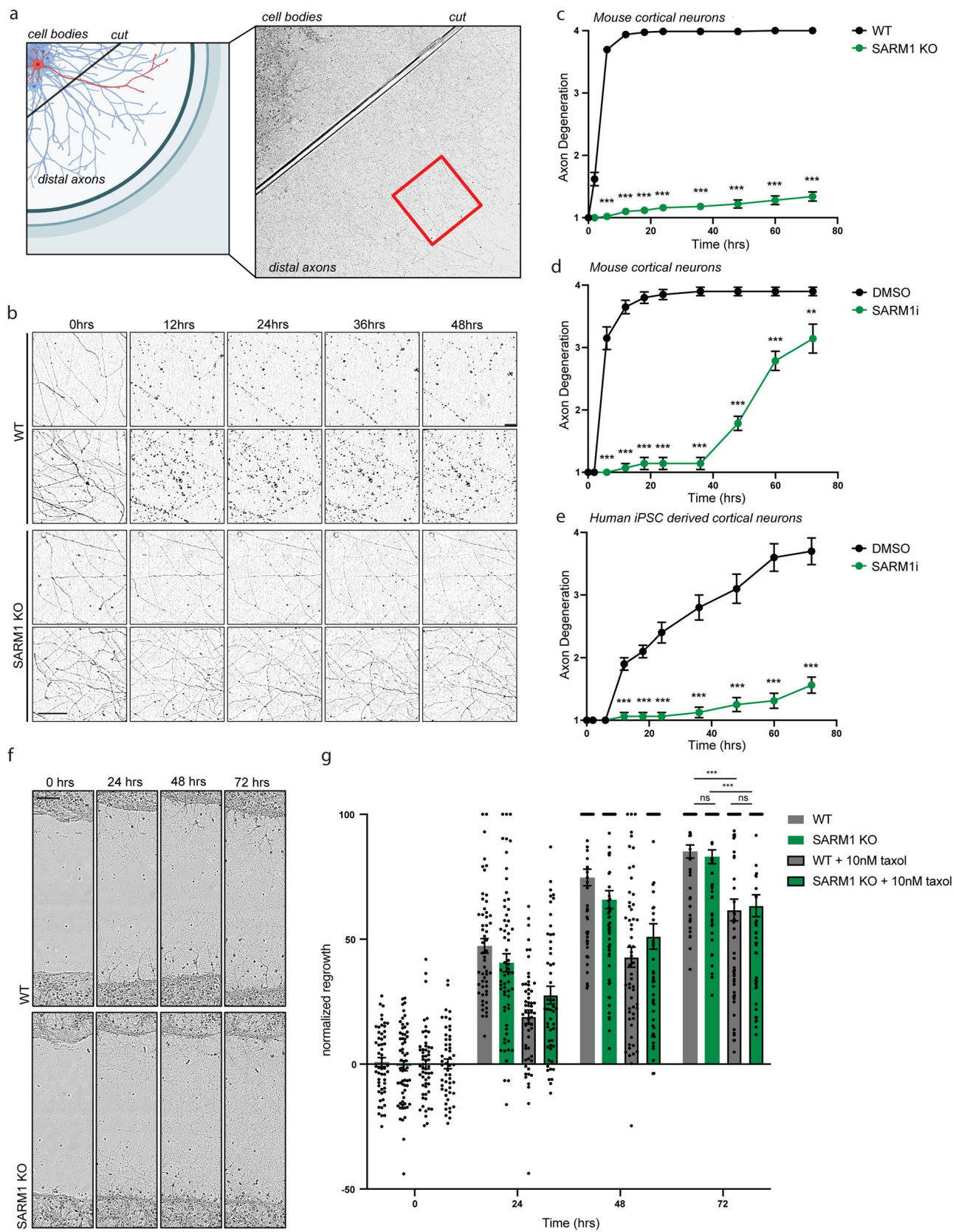


Figure 1. SARM1-dependent axon degeneration in cortical neurons. **a**, Schematic of spot culture used for axon degeneration imaging after injury. **b**, Sample images and **(c)** quantification of axon degeneration in WT and SARM1 KO mouse cortical neurons after injury ($n = 49\text{--}79$ images/condition; Mann–Whitney test; $***p < 0.001$ for all time points after 2 h). See Extended Data Figures 1–1–1–3 for additional information on the axon degeneration scoring algorithm. Quantification of axon degeneration after treatment with 10 μ M SARM1 inhibitor or DMSO in either mouse ($n = 14\text{--}20$ images/condition; Mann–Whitney test, $**p < 0.01$, $***p < 0.001$; **d**) or human ($n = 10\text{--}16$ images/condition; Mann–Whitney test; $***p < 0.001$; **e**) cortical neurons. Sample images **(f)** and quantification **(g)** of neurite regrowth after injury in WT or SARM1 KO cortical neurons treated with DMSO or 10 nM taxol ($n = 50\text{--}62$ images/condition; two-way ANOVA, multiple comparisons; $***p < 0.001$). Scale bars, 100 μ m. See Extended Data Table 1–1 for further statistical analysis.

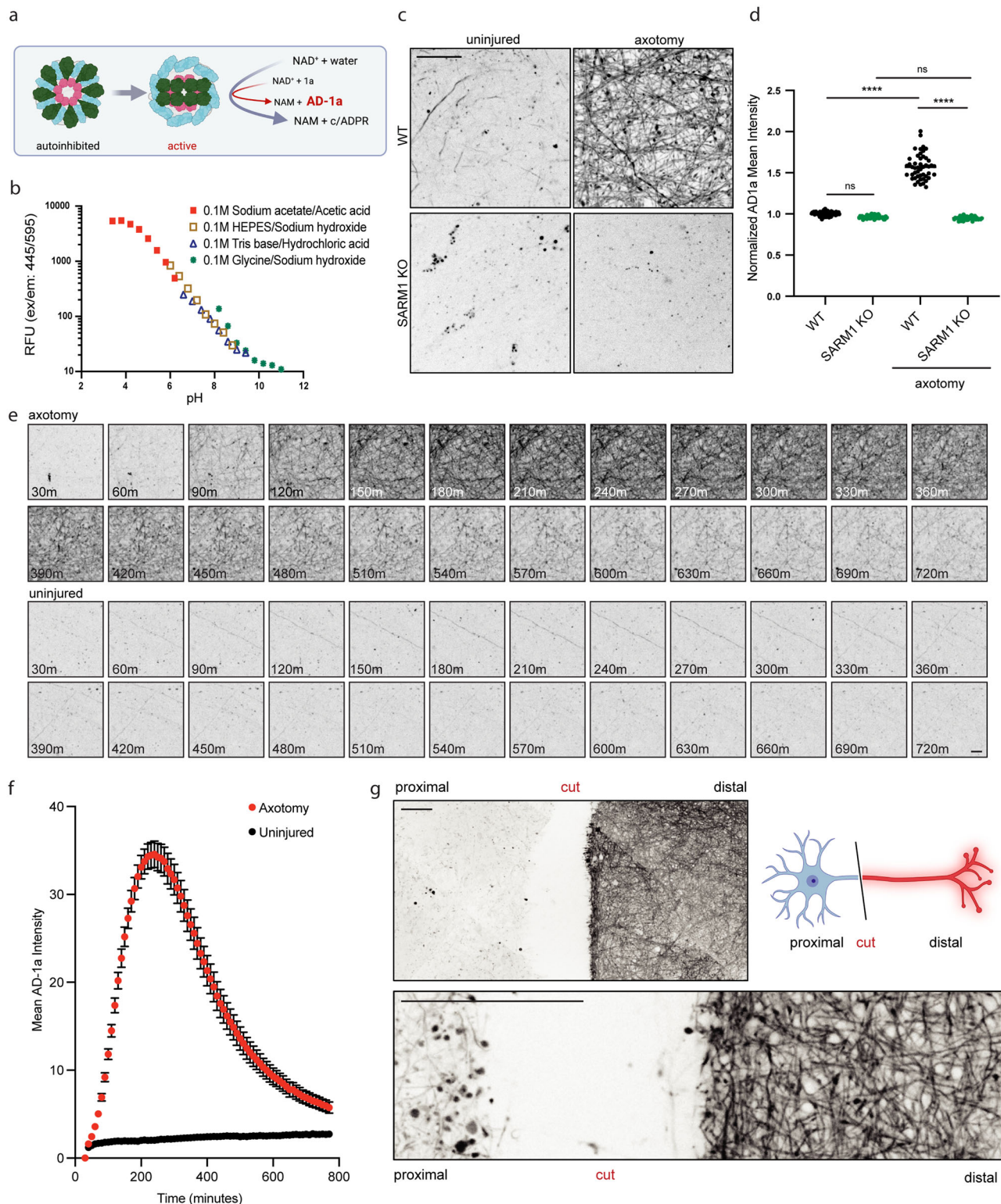


Figure 2. SARM1 is activated in axons distal, but not proximal, to injury site. **a**, Schematic of hydrolysis of NAD⁺ to NAM and ADPR/cADPR or base-exchange reaction of NAD⁺ and 1a to NAM and fluorescent probe AD-1a catalyzed by SARM1. **b**, AD-1a autofluorescence with pH in different buffer conditions. **c**, Sample images and **(d)** quantification of AD-1a fluorescent in axons distal to the injury site 4 h after injury in WT or SARM1 KO mouse cortical neurons ($n = 44\text{--}75$ images/condition; Tukey's multiple-comparison test; **** $p < 0.0001$). Scale bar, 20 μm. Sample images **(e)** and quantification ($n = 30$ images/condition; Mann–Whitney test; *** $p < 0.001$ for all time points after 60 min; **f**) of time course of AD-1a fluorescence in axons after injury (top) or control (bottom) in WT mouse cortical neurons. Scale bar, 20 μm. **g**, AD-1a fluorescence proximal and distal to the injury site in WT mouse cortical neurons 4 h after injury. Scale bar, 50 μm. See Extended Data Figure 2-1 for uncropped images.

axons after injury but is not detected in injured SARM1 KO axons (Fig. 2*c,d*). Some AD-1a background signal could be detected in both WT and SARM1 KO neurons, which most likely

resulted from 1a pH-dependent fluorescence in acidic vesicular compartments. Interestingly, SARM1 activation, as visualized by AD-1a fluorescence, is first detected in mouse cortical axons

~60 min after injury and then increases in intensity and prevalence until ~4 h after injury (Fig. 2*e,f*). In line with previous results showing that axons undergo morphological degeneration and fragmentation before 6 h after injury, AD-1a fluorescence begins to decrease at a similar time point, likely as a result of membrane rupture and release of the membrane-impermeable fluorescent probe into the media.

Next, we investigated the subcellular localization of SARM1 activation upon injury. As can be observed by AD-1a fluorescence 4 h after injury, SARM1 activation is restricted specifically to the axonal compartment distal to the injury site, with an almost complete absence of any AD-1a fluorescence in the axons proximal to the site of injury (Fig. 2*g*, Extended Data Figure 2-1). This is in line with the observation that there is no morphological axon degeneration proximal to the injury site and cell bodies of injured cortical neurons do not undergo degeneration in response to this type of mechanical injury. Therefore, AD-1a is a powerful tool to visualize SARM1 activity in subcellular compartments over time. In addition, these experiments show that SARM1 activation is initiated as early as 1 h after injury and is restricted to axonal compartments distal to the injury site in cortical neurons.

Vacor derivative VMN is a SARM1-specific agonist

SARM1 has been shown to be a metabolic sensor and is activated by a change in the ratio of NMN to NAD⁺, which both bind to the same allosteric site on the ARM domain of SARM1 (Bratkowski et al., 2020; Jiang et al., 2020; Sporny et al., 2020; Figley et al., 2021). When NMN levels increase, NMN can displace NAD⁺ to induce a conformational change in SARM1 and thereby activate the enzyme (Fig. 3*a*). In mouse cortical neurons, we find that CZ-48, a cell membrane-permeable mimetic of NMN (Zhao et al., 2019), in combination with FK866, a nicotinamide phosphoribosyltransferase (NAMPT) inhibitor, which leads to decreased NAD⁺ levels, will lead to SARM1-dependent axon degeneration (Fig. 3*b*). In contrast to other cell types (Zhao et al., 2019; Figley et al., 2021), even high concentrations of CZ-48 by itself do not cause degeneration in WT cortical neurons. However, high concentrations or prolonged exposure of FK866 can cause SARM1-independent axon degeneration and cell death, as NAD⁺ biosynthesis is inhibited and NAD⁺ stores are depleted (Extended Data Figure 3-1*e*).

Previous work has indicated that treatment with the rodenticide vacor activates SARM1 (Loreto et al., 2021). Specifically, the NAMPT-generated vacor metabolite VMN, which is structurally similar to NMN, activates SARM1. Consistent with previous results in sensory neurons and retinal ganglion cells (Loreto et al., 2021), treatment with the rodenticide vacor leads to SARM1-dependent axon degeneration in both mouse and human cortical neurons (Fig. 3*c,d* and Extended Data Figure 3-1*f,g*), making it a reliable tool to study the downstream effects of SARM1 activation. When cotreating vacor with the NAMPT inhibitor FK866, we see the inhibition of axon degeneration in WT cortical neurons in a dose-dependent manner (Extended Data Figure 3-1*a-e*). These results confirm that SARM1-dependent axon degeneration induced by vacor in cortical neurons requires NAMPT activity.

Global SARM1 activation in mouse cortical neurons causes NAD⁺, ATP, and mitochondrial membrane potential loss, followed by cell body and axon degeneration and NfL release
SARM1 is localized to the outer mitochondrial membrane (Gerdtz et al., 2013; Miyamoto et al., 2024) and is present in both axons and cell bodies of cortical neurons. Using vacor as a noncell compartment-specific SARM1 activator, we next investigate the

downstream effects of global SARM1 signaling in cortical neurons. In contrast to axonal injury, the addition of 5 μM vacor causes rapid SARM1 activation, as indicated by AD-1a fluorescence at 4 h after treatment, in both the cell body and the axonal compartments (Fig. 3*e,f*). Vacor-induced AD-1a fluorescence gain is SARM1-dependent, again confirming both that AD-1a is a SARM1-specific probe and that vacor is a SARM1 agonist. In mouse primary cortical cultures, not all cell bodies appear to show AD-1a fluorescence upon vacor stimulation (Fig. 3*e*). As these cultures also contain a small subset of glial cells, in particular astrocytes, and neither astrocytes nor microglia express SARM1 or show AD-1a fluorescence after vacor treatment, it is likely that the nonresponsive cell bodies correspond to glial cells (Extended Data Figure 3-2).

In line with SARM1 activation in the cell body and in contrast to mechanical axonal injury, vacor treatment leads to SARM1-dependent cell body death, as measured by the uptake of a cell membrane-impermeable nuclear dye (Fig. 3*g*). SARM1 activation by vacor treatment in cortical neurons results in rapid loss of mitochondrial membrane potential (Fig. 3*h,i*), NAD⁺ (Fig. 3*j*), and ATP levels (Fig. 3*k*). By 16 h after vacor treatment and shortly after onset of morphological axon degeneration, we detect an increase of the biomarker NfL in the media (Fig. 3*l*). Taken together, we show that SARM1 activation in mouse cortical neurons leads to rapid loss of NAD⁺ and ATP levels, as well as mitochondrial membrane potential, followed by axon degeneration, cell body death, and NfL release.

cADPR, a Ca²⁺-mobilizing messenger, stimulates the release of Ca²⁺ from internal stores (Guse, 2004). This in turn may activate calpains, calcium-dependent proteases, and initiate the final steps in the axon degeneration cascade (Extended Data Figure 3-3*a*). Whether NAD⁺ loss by itself or in combination with increased levels of cADPR is the mechanism by which SARM1 causes axon degeneration remains unclear. We find that in mouse cortical neurons, supplementation with NAD⁺ or the NAD⁺ precursor nicotinamide delays injury-induced axon degeneration and prevents vacor-induced cell body death (Extended Data Figure 3-3*b,c*). However, treatment with the cADPR antagonist 8-Br-cADPR, which was used by Y. Li et al. (2022) to reduce paclitaxel-induced axon degeneration in mouse sensory neurons, has no effect on either (Extended Data Figure 3-3*d,e*) under our experimental conditions.

Furthermore, ADPR and cADPR are both agonists of the Ca²⁺-permeable nonselective cation channel, TRPM2 (Okada et al., 2023). Therefore, we hypothesized that TRPM2 may play an important role downstream of SARM1 activation, again contributing to Ca²⁺ influx and calpain activation, and that loss of TRPM2 may slow morphological axon degeneration. However, we find that loss of TRPM2 delays neither axon degeneration to a variety of different SARM1-activating cell stressors nor vacor-induced cell body death (Extended Data Figure 3-3*f-k*) in mouse cortical neurons. Therefore, it seems likely that in cortical neurons, the loss of NAD⁺ level is the predominant cause of SARM1-dependent axon degeneration and subsequent loss of ATP levels lead to channel failure, calcium influx, calpain activation, and axon degeneration.

Neither SARM1 loss nor activation results in global proteomic changes

The effects of SARM1 on NAD⁺ levels and the downstream consequences on cellular metabolism have been established (Ko et al., 2021). However, whether SARM1 loss or activation alters protein levels in neurons has so far not been described. WT or SARM1 KO mouse cortical neurons were cultured for 9 d and treated with

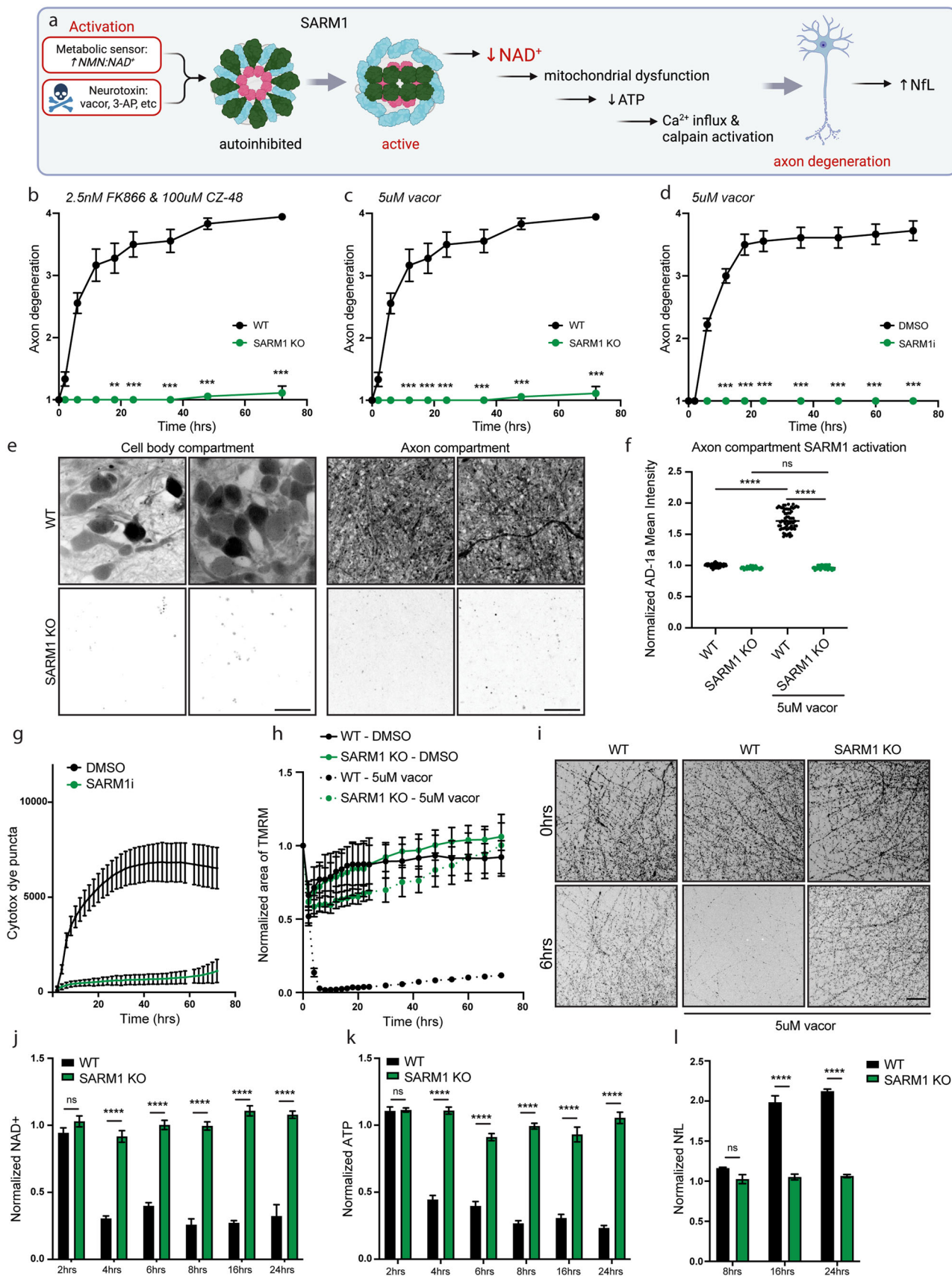


Figure 3. Vacor selectively activates SARM1 to induce axon degeneration in mouse cortical neurons. **a**, Schematic of SARM1 activation and downstream events. Quantification of axon degeneration after treatment of WT or SARM1 KO mouse cortical neurons with **(b)** 100 μ M CZ-48 and 2.5 nM FK866 ($n = 21$ – 22 images/condition; Mann–Whitney test; $^{**}p < 0.01$; $^{***}p < 0.001$) or **(c)** 5 μ M vacor ($n = 18$ images/condition; Mann–Whitney test; $^{***}p < 0.001$ for all time points after 6 h). See Extended Data Figure 3-1 for data on cotreatment of mouse cortical cultures with vacor and FK866. **d**, Quantification of axon degeneration after treatment of WT mouse cortical neurons with 5 μ M vacor in the presence of 10 μ M SARM1 inhibitor ($n = 12$ – 18 images/condition;

either DMSO or 5 μ M vacor for 4 h. Cell pellets were collected, and samples were analyzed by a MS-based quantitative proteomics method employing multiplexed isobaric labeling and real-time search-directed quantification. The resulting data were further analyzed by MSstats to determine differentially regulated proteins.

When comparing WT to SARM1 KO proteome, we detect only a handful of proteins that are significantly changed (Fig. 4*a*). Specifically, we confirmed the loss of SARM1 in SARM1 KO neurons and detected decreased levels of RNF167, Schlafen Family Member 9 (SLFN9), the homolog of human Schlafen Family Member 13 (SLFN13), and Kinesin Family Member 1C (KIF1C; Fig. 4*c–f*). However, known downstream targets of RNF167, such as ADP ribosylation factor like GTPase 8 (ARL8) and Vesicle-Associated Membrane Protein 3 (VAMP3; Yamazaki et al., 2013), are not altered (Extended Data Figure 4-1*c–e*), and other members of the Kinesin Family are also unchanged (Extended Data Figure 4-1*f–h*). Furthermore, Rap Guanine Nucleotide Exchange Factor 4 (RPGF4) protein levels are increased in SARM1 KO cortical neurons specifically (Fig. 4*g*). Differences in hemoglobin E and hemoglobin Y (Q9CR49) are driven mainly by one outlier and may therefore not represent true biological differences (Fig. 4*h,i*). These findings confirm that constitutive loss of SARM1 does not lead to global proteomic changes in cortical neurons.

Activation of SARM1 by vacor treatment resulted in even fewer proteomic changes (Fig. 4*b*). Tankyrase 2 (TNKS2), the poly-ADP-ribosyltransferase also known as PARP5b, was specifically upregulated with SARM1 activation in WT neurons, while Zinc Finger Protein 607B (G3X9H3) was upregulated with vacor treatment in both WT and SARM1 KO neurons (Fig. 4*j,k*). Interestingly, Tankyrase 1 shows similar, though not proteome-wide significant, changes with SARM1 activation in WT neurons (Fig. 4*l*), while other PARPs do not (Fig. 4*m,n*).

Of the proteomic changes detected by MS, only decreased levels of RNF167 in SARM1 KO cortical neurons were validated using immunoblotting (Extended Data Figure 4-1*a,b*). Interestingly, the RNF167, SLFN9, and KIF1C are all located close to the gene locus of SARM1 on chromosome 11, and the decrease of these proteins may therefore be a result of passenger mutations in this genetic model (Uccellini et al., 2020; Doran et al., 2021). Other known passenger mutations in this mouse line, such as XIAP-Associated Factor 1 (XAF1), were not identified, likely due to low expression in neurons. Furthermore, members of the NAD⁺ biosynthetic pathway, such as NAMPT and NMNATs, or NAD⁺-consuming proteins, such as Sirtuins, were not altered in these experiments (Fig. 4*o–q*; Extended Data Figure 4-1*i–m*). Overall, very few proteomic changes were detected with either SARM1 loss or activation, further confirming that SARM1 acts mainly by effecting axon degeneration at the metabolite level and does not have broad effects on protein homeostasis before onset of cell death.

Microtubule and mitochondrial dysfunction cause SARM1-dependent axon degeneration and SARM1-independent cell body death

To investigate whether other types of cell stress lead to global or local SARM1-dependent axon degeneration, we treated mouse cortical neurons with vincristine, taxol, or rotenone. Vincristine is a microtubule-destabilizing agent which acts by binding to both free and microtubule-associated tubulin. In contrast, taxol is a microtubule-stabilizing agent suppressing microtubule dynamics. Both vincristine and taxol likely alter axon transport and thereby levels of NMNAT2, which in turn has been shown to regulate SARM1 activity (Figley et al., 2021). While treatment with 100 nM vincristine induced rapid and complete axon degeneration in WT mouse cortical neurons, this was significantly reduced in SARM1 KO neuron (Fig. 5*a,b*). Treatment with 100 nM taxol, in contrast, led to slow axon degeneration in WT neurons, which was only delayed but not prevented with SARM1 KO (Fig. 5*c,d*), indicating that taxol-induced axon degeneration may depend on additional cell stress-response pathways.

Rotenone disrupts the electron transport chain complex I in mitochondria, causing mitochondrial dysfunction (Chan et al., 2005), and likely activates SARM1 by altering NMN:NAD⁺ ratios. Like vincristine treatment, treatment with 250 nM rotenone caused swift axon degeneration in WT neurons, which was significantly reduced in SARM1 KO neurons (Fig. 5*e,f*). SARM1 small-molecule inhibition results in similar delays in axon degeneration in response to these stressors (Fig. 5*g–i*) during the first 48 h after stress. However, after ~40–48 h, axon degeneration in response to vincristine and rotenone is not inhibited by SARM1 small-molecule inhibition to the same extent as SARM1 KO, possibly due to incomplete inhibition of SARM1 with the tested inhibitor concentrations.

In response to axon injury distal to the axon initiation site, we did not observe cell body degeneration, while in response to direct SARM1 activation by vacor, we observed SARM1-dependent cell body death. In contrast, both WT and SARM1 KO neurons showed similar kinetics and degree of cell body death in response to vincristine, taxol, and rotenone treatment (Fig. 5*j–l*). This is especially interesting as previous work by Summers et al. (2014) found that mitochondrial stress-induced cell body death in DRG neurons is SARM1-dependent, further highlighting differences in degeneration in neurons of the central and peripheral nervous system and the need to study these fundamental degenerative mechanisms in a variety of neuronal subtypes. Therefore, these experiments reveal that cell body death in mouse cortical neurons in response to microtubule and mitochondrial dysfunction is SARM1-independent.

SARM1 activation occurs predominantly in axons, not cell bodies, in response to injury and cell stress

While vincristine and rotenone treatments cause fast axon degeneration in WT cortical neurons which is greatly inhibited

←
Mann–Whitney test; *** $p < 0.001$ for all time points after 6 h). See Extended Data Figure 3-1 for data on vacor treatment of human iPSC-derived neurons. **e**, Sample images of AD-1a fluorescence after 4 h of 5 μ M vacor treatment in WT or SARM1 KO mouse cortical neurons in either the cell body (left) or axon (right) compartment. Scale bar, 20 μ m. See Extended Data Figure 3-2 for characterization of mouse cortical culture cell-type composition and glial culture AD-1a fluorescence after vacor treatment. **f**, Quantification of AD-1a fluorescence after 4 h of 5 μ M vacor treatment in WT or SARM1 KO mouse cortical neurons in the axon compartment ($n = 44–75$ images/condition; Tukey's multiple-comparison test; **** $p < 0.0001$). Experiments were run in parallel with axotomy conditions (Fig. 2*d*), and the same control was used for both conditions. **g**, Quantification of cytotox dye-labeled puncta in dissociated WT or SARM1 KO cortical neurons after treatment with 5 μ M vacor ($n = 20$ images/condition; Mann–Whitney test; *** $p < 0.001$ for all time points after 4 h). Quantification (**h**) and sample images (**i**) of TMRM fluorescence in axons after 5 μ M vacor treatment ($n = 5–8$ images/condition; Mann–Whitney test; *** $p < 0.001$ for all time points after 4 h for WT + vacor compared with SARM1 KO + vacor). Scale bar, 100 μ m. Time course of normalized NAD⁺ (**j**), ATP (**k**), and Nfl (**l**) levels after 5 μ M vacor treatment in WT mouse cortical neurons ($n = 4–8, 6–20$, and 4 measurements/condition, respectively; Šidák's multiple-comparison test; **** $p < 0.0001$). See Extended Data Figure 3-3 for data on axon degeneration and cell body death after stress in mouse cortical cultures treated with NAD⁺, nicotinamide, and 8-Br-cADPR or in mouse cortical cultures from TRPM2 KO animals. See Extended Data Table 1-1 for further statistical analysis.

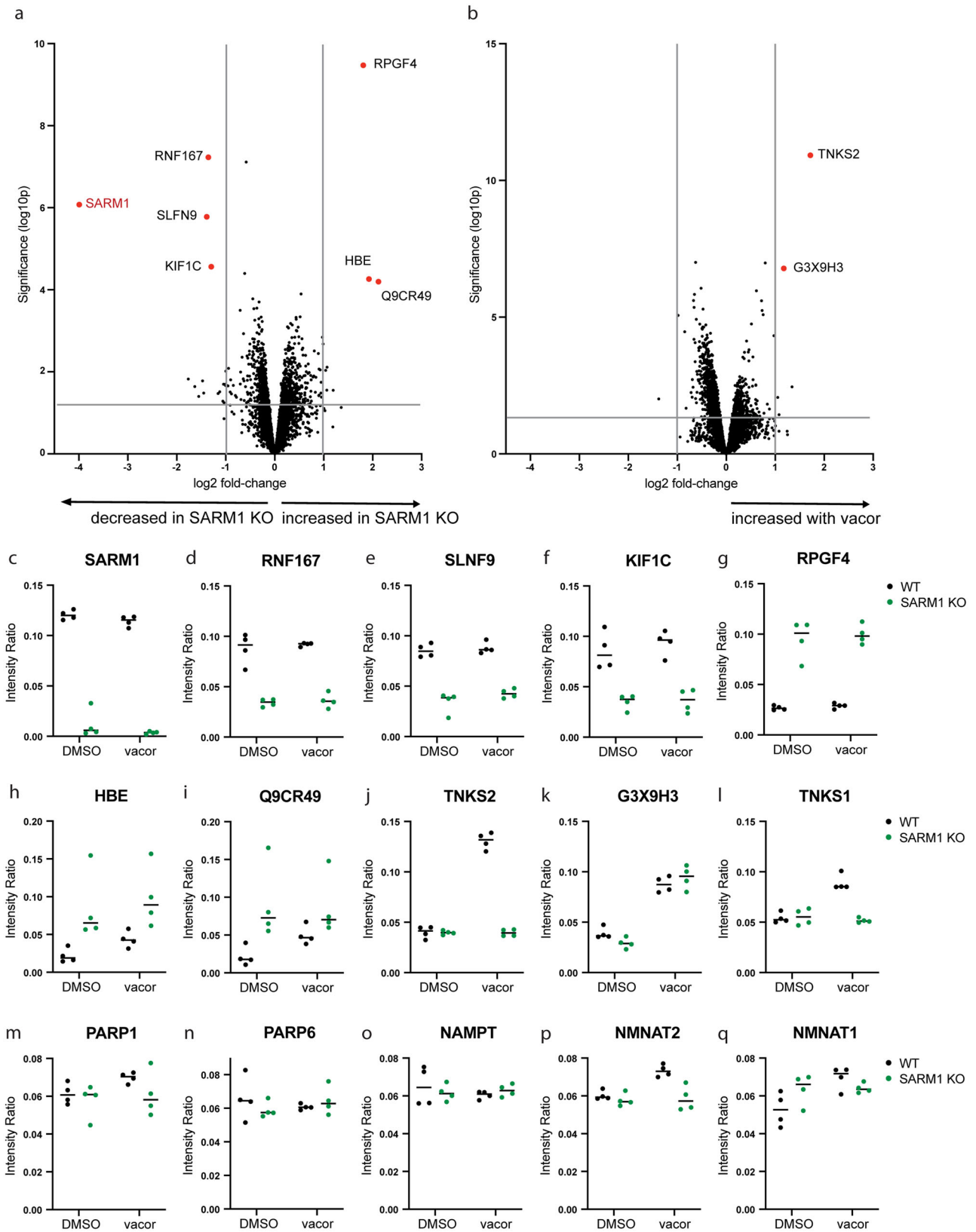


Figure 4. SARM1 KO or activation in mouse cortical neurons results in only minor proteomic changes. **a**, MS analysis of peptide fragment abundance in lysates of WT or SARM1 KO mouse cortical neurons. **b**, MS analysis of peptide fragment abundance in lysates of WT mouse cortical neurons treated for 4 h with 5 μ M vacor or DMSO. Quantification of peptide abundance as measured by MS of proteins altered in SARM1 KO (**c–f**), or with SARM1 activation in WT (**j,k**), or related to SARM1 or SARM1 proteomic hit biology (**l–q**) in WT or SARM1 KO+/- 5 μ M vacor treatment. $n = 4$ replicates/condition. See Extended Data Figure 4-1 for immunoblot quantification of RNF167 levels in WT and SARM1 KO cortical cultures and quantification of peptide abundance as measured by MS of other proteins of interest.

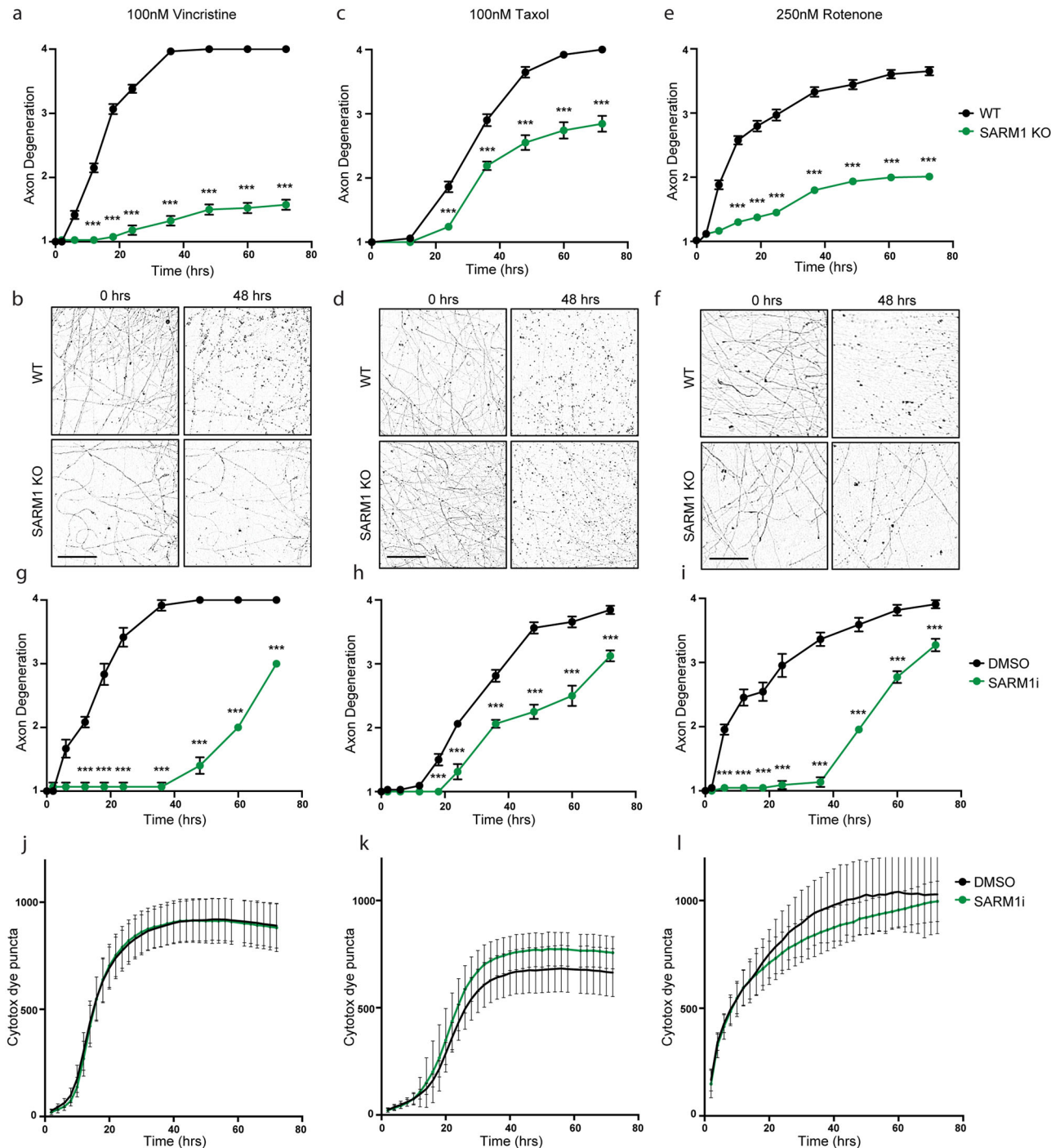


Figure 5. Microtubule dysregulation and mitochondrial stress cause SARM1-dependent axon degeneration and SARM1-independent cell body death. Sample images and quantification of axon degeneration in WT or SARM1 KO mouse cortical neurons after treatment with 100 nM vincristine (**a,b**), 100 nM taxol (**c,d**), or 250 nM rotenone (**e,f**; scale bar, 100 μ m; $n = 40$ – 60 , 51 – 58 , and 80 – 86 images/condition, respectively; Mann–Whitney test; $***p < 0.001$). Quantification of axon degeneration in WT mouse cortical neurons treated with 10 μ M SARM1 inhibitor and 100 nM vincristine (**g**), 100 nM taxol (**h**), or 250 nM rotenone (**i**; $n = 12$ – 15 , 16 – 32 , 20 images/condition, respectively; Mann–Whitney test; $***p < 0.001$). Quantification of cytotox dye puncta in WT mouse cortical neurons treated with 10 μ M SARM1 inhibitor and 100 nM vincristine (**j**), 100 nM taxol (**k**), or 250 nM rotenone (**l**). $n = 32$, 32 , and 10 images/condition, respectively.

by SARM1 loss, taxol mediates slower axon degeneration which is only partially rescued by SARM1 loss. Using AD-1a, we investigate SARM1 activation in axons following vincristine, taxol, and rotenone treatment. Similar to axonal injury and direct SARM1 activation in response to vacor treatment, all three stress treatments lead to significant increases in AD-1a fluorescence in the axonal compartment of WT, but not SARM1 KO cortical neurons (Fig. 6*a–d*). However, while axonal injury and vacor

treatment cause an approximately twofold increase in AD-1a fluorescence in mouse cortical neurons, AD-1a fluorescence is only elevated $\sim 30\%$ in response to vincristine and rotenone treatment and $\sim 10\%$ in response to taxol treatment. In human cortical neurons, these different cell stressors similarly result in axonal SARM1 activation (Extended Data Figure 6-1*a,b*). While vacor treatment leads to high levels of AD-1a fluorescence within 4 h of treatment, vincristine and rotenone cause intermediate

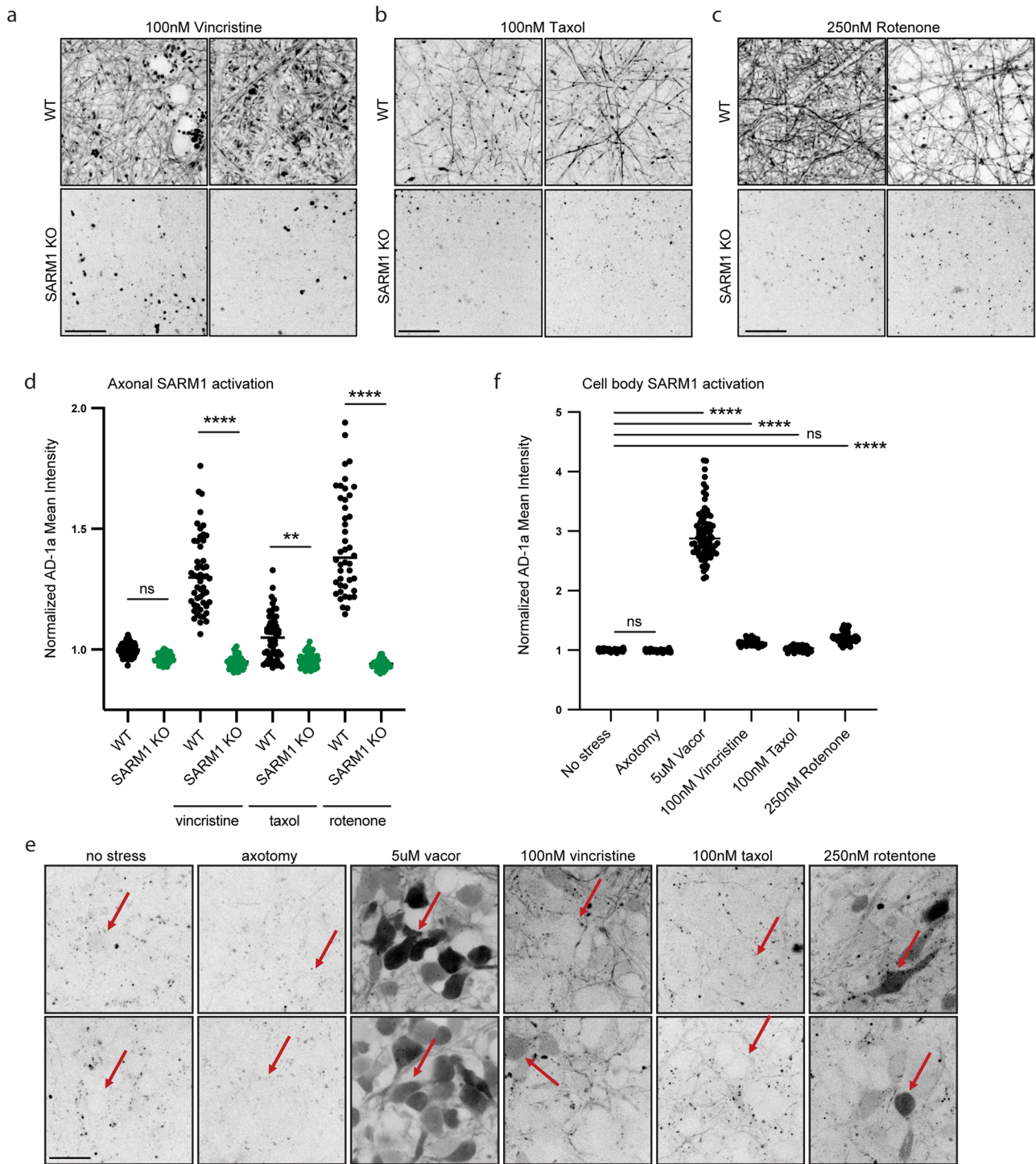


Figure 6. Localization of SARM1 activation is dependent on the type of cellular stressor. Sample images (**a–c**) and quantification (**d**) of AD-1a fluorescence in WT or SARM1 KO mouse cortical neurons after 4 h treatment with 100 nM vincristine, 100 nM taxol, or 250 nM rotenone. Scale bar, 20 μ m; $n = 44–75$ images/condition. Sample images (**e**) and quantification (**f**) of AD-1a fluorescence in cell bodies of WT mouse cortical neurons after stress treatment. Arrowheads denote cell bodies; scale bar, 20 μ m; $n = 80–88$ images/condition. Two-way ANOVA, multiple comparisons; ** $p < 0.01$; **** $p < 0.0001$. See Extended Data Figure 6-1 for sample images adjusted to equal brightness and contrast and AD-1a fluorescence in human iPSC-derived cortical neurons after stress.

AD-1a fluorescence, and taxol causes only sparse SARM1 activation in axons after 24 h.

We have previously shown that global SARM1 activation by vacor treatment causes AD-1a fluorescence in cell bodies and cell body degeneration, while axon injury distal to the axon initiation site does not. Next, we characterize SARM1 activation

in response to microtubule and mitochondrial dysfunction induced by vincristine, taxol, and rotenone treatment in the cell body compartment. To be able to show AD-1a signal across all conditions, we decreased the brightness and contrast of the vacor condition in comparison with all other conditions, which were kept constant (Fig. 6e). Sample images of equal brightness

and contrast are shown in Extended Data Figure 6-1b. Interestingly, vincristine and rotenone treatments cause only minor AD-1a fluorescence in cell bodies, while taxol treatment does not result in any AD-1a fluorescence in cell bodies (Fig. 6e, f). This is in line with our previous finding that cell body death in response to these stressors is SARM1-independent and indicates that other cell stress-response pathways drive this phenotype. The background signal observed is SARM1-independent and, as mentioned previously, likely AD-1a autofluorescence from low pH cellular vesicles. Together, these experiments show that SARM1 activation can be localized to specific neuronal compartments depending on the type of stressor.

Discussion

SARM1 is the central executioner of Wallerian degeneration, originally defined as the process of organized axon self-destruction distal to the injury site. The term is typically used to describe axon degeneration in neurons of the peripheral nervous system, and SARM1 function has mainly been studied in mouse DRG sensory neurons (Summers et al., 2014; Bosanac et al., 2021). We demonstrate directly that in both mouse and human cortical neurons, SARM1 is activated in response to a number of different stress stimuli not previously investigated in this neuronal subtype. As a first, this study finds that the localization of SARM1 activation is dependent on the type of stressor and leads to SARM1-dependent axon degeneration and, in the case of microtubule and mitochondrial dysfunction, SARM1-independent cell body degeneration.

SARM1 functions as an autoinhibited NADase that once activated initiates axon degeneration by hydrolyzing NAD^+ , which in turn results in metabolic catastrophe, setting off a cascade of downstream processes ending in morphological axon degeneration. It has been shown that germline loss of SARM1 causes elevation of NAD^+ levels in the brain (Sasaki et al., 2020). However, whether this increase in NAD^+ levels results in changes in protein homeostasis or whether SARM1 has other functions that may affect the global neuronal proteome has not been investigated. Here we find that the expression levels of very few proteins are altered in mouse cortical neurons with constitutive SARM1 loss, which is in stark contrast to other neuronal stress pathways that induce broad transcriptional and translational responses (Watkins et al., 2013; Tortosa et al., 2022).

While it is known that SARM1 activation rapidly decreases NAD^+ levels, we were also interested in whether SARM1 activation leads to concomitant proteomic changes. As we wanted to avoid characterizing the proteomic signature of late-stage neuron degeneration or SARM1 activation-independent changes, we used vacor to directly activate SARM1 and collected lysates before onset of significant morphological changes. As in the case of SARM1 loss, SARM1 activation causes very few protein expression changes, confirming that SARM1 exerts its effect mainly at the metabolic level. Only TNKS2, also known as Parp5b, was significantly increased with SARM1 activation in WT neurons specifically, while TNKS1, also known as Parp5a, trended in the same direction. Tankyrases consume NAD^+ to catalyze the ADP ribosylation of a number of different target proteins, thereby regulating various cellular processes such as DNA damage response and Wnt and Notch signaling (Sagathia et al., 2023). How SARM1 activation results in TNKS2 increases, and whether this contributes to axon degeneration, is unclear and requires further investigation.

To study axon degeneration in cortical neurons, we developed a medium-throughput experimental pipeline. Neuron “spots” are

plated in a 48-well tissue culture plate, which allows for injury of axons and separate imaging of cell bodies and axons. We find that the axon degeneration state can be reliably captured using phase imaging only. Restricting axon degeneration imaging to phase eliminates the need for overexpression of fluorescent markers, which may artificially perturb the cell or fixation and immunofluorescence staining, which would prevent live, time-lapse imaging. Using an automated imaging system housed in a tissue culture incubator, multiple images per well are acquired automatically every 2 h over a period of 3 d. This allows for tracking of axon morphology over time with minimal experimenter effort.

To quantify axon degeneration, we developed a custom deep learning algorithm based on two convolutional neural networks: a unary model, which takes as input a single image and outputs a probability for each of the four possible axon degeneration scores, as well as a transition model, which takes as input a pair of images from the same field of neurons at consecutive time points and predicts the probability of the score change between the two images. Using both of these measures, we then generate the optimal score sequence over time. The algorithm is robust and works well on images that also contain fields of cell bodies and artifacts of axonal injury, such as grooves in the tissue culture plastic created by the microblade. This eliminated the need to manually set fields of view before imaging or crop images during image postprocessing to contain only fields of axons. Combining the use of an abundant neuronal cell type, automated imaging, and AI-assisted scoring, a single automated imaging instrument can reliably test over 500 different conditions on primary neurons within a week with minimal experimenter time.

Using this semiautomated pipeline, we studied axon degeneration in both mouse primary cortical neurons and human iPSC-derived cortical neurons in response to a number of different stressors. While Osterloh et al. (2012) have previously shown that mouse cortical neurons undergo SARM1-dependent axon degeneration after mechanical injury, we demonstrate in this study that injury also results in rapid axon degeneration in human culture systems. However, in mouse cortical neurons, initial signs of morphological degeneration occur between 2 and 6 h, and axons are completely degenerated within 24 h, while in human cortical neurons, morphological axon degeneration is initiated between 6 and 12 h, and axon degeneration proceeds more slowly, reaching completion by 3 d. Furthermore, while only 5 μM vacor is needed to induce rapid and complete axon degeneration in mouse cortical neurons, 10-fold higher concentrations are required in human cortical neurons. The differences in axon degeneration kinetics, not previously characterized, may be due to differences in media composition, which for the human culture system were optimized to enable the study of these neurons for weeks and months and were supplemented with neurotrophic factors such as BDNF to support culture longevity. Independently, there may be differences in endogenous levels of NMN and NAD^+ , NMNAT2 and its regulation, and SARM1 expression and activity between neurons from different species, as well as between different neuronal subtypes within a species. It will be critical to understand the cross-species and cross-neuronal subtype differences, as this will impact which neuronal populations may be vulnerable to SARM1 activation in different disease or stress conditions and which model organisms can be used to accurately model therapeutic SARM1 inhibition approaches.

We show here that the kinetics of axon degeneration and the subcellular localization of SARM1 activation are stressor dependent. Axon injury results in localized SARM1 activation in the

axon segments distal to the injury site and rapid degeneration of only the axonal compartment, not the cell body. In contrast, after vacor treatment, SARM1 activation occurs in both axons and cell bodies causing fast, SARM1-dependent degeneration of both compartments. Vincristine, which destabilizes microtubules, and rotenone, which causes mitochondrial dysfunction, both induce strong SARM1 activation in axonal compartments and only sparse SARM1 activation in cell bodies and result in rapid, SARM1-dependant axon degeneration. Taxol, which stabilizes microtubules, only results in weak SARM1 activation in axons and causes slow axon degeneration, which is only partially inhibited by the loss of SARM1. Taxol treatment does not result in any SARM1 activation in cell bodies at the time points we investigated. While microtubule and mitochondrial dysfunction cause cell body death, as measured by the uptake of a cell membrane-impermeable nuclear dye, this is not SARM1-dependent. Therefore, we demonstrate here for the first time that SARM1 activation correlates with axon degeneration kinetics, where SARM1 can cause rapid axon degeneration, but activation of other cell stress pathways may result in slow, SARM1-independent degeneration. Furthermore, we demonstrate that SARM1, which is present on mitochondria throughout the neurons (Miyamoto et al., 2024), can be activated in specific subcellular compartments depending on the stress signal.

How do these different stressors cause localized SARM1 activation? Injury has been shown to affect NMNAT2 levels distal to the injury site in axons (Gilley and Coleman, 2010). NMNAT2 regulates NMN:NAD⁺ ratios, which in turn affect SARM1 activation. Therefore, the finding that SARM1 activation after injury is localized to axonal segments distal to the injury site is expected. In contrast, the vacor metabolite VMN directly binds to an allosteric site on SARM1 to cause a conformational change and activation (Loreto et al., 2021). Vacor treatment leads to global SARM1 activation throughout the neuron and SARM1-dependent axon and cell body degeneration. Vincristine and taxol, which cause microtubule dysfunction and impact axon trafficking, likely affect NMNAT2 levels and therefore NMN:NAD⁺ in axon compartment specifically, resulting in SARM1 activation in these compartments, but not in the cell body. In contrast, rotenone-induced mitochondrial dysfunction may directly affect NMN:NAD⁺ ratios. However, it does not lead to robust SARM1 activation in cell bodies. Possibly, the concentrations of NMN and NAD⁺ differ in the axon and cell body compartments, and therefore the level of mitochondrial dysfunction required to activate SARM1 may also differ. Alternatively, it has been suggested that mitochondrial dysfunction can affect NMNAT2 trafficking (Loreto et al., 2020), which would explain the similar SARM1 activation pattern as observed with microtubule dysfunction.

Microtubule and mitochondrial dysfunction both result in SARM1-independent cell death, suggesting that other cell death pathways, such as JNK signaling, may play an important role. A great deal of excitement is currently being generated around therapeutic approaches that regulate NAD⁺ levels, either by NAD⁺ supplementation, NMNAT2 activation, or SARM1 inhibition. However, our study shows that while these strategies may be beneficial in clinical indications where axon degeneration is the driving force of disease pathology, they may be less successful in instances where other cell stress pathways are concomitantly activated to cause SARM1-independent cell death. Understanding the neurodegenerative diseases in which SARM1 activation plays a major role and exploring combination therapy approaches which protect both the cell body and the axon compartment will be critical to develop successful NAD⁺-regulating therapies.

References

- Angeletti C, Amici A, Gilley J, Loreto A, Trapanotto AG, Antoniou C, Merlini E, Coleman MP, Orsomando G (2022) SARM1 is a multi-functional NAD(P)ase with prominent base exchange activity, all regulated by multiple physiologically relevant NAD metabolites. *iScience* 25:103812.
- Avraham O, Le J, Leahy K, Li T, Zhao G, Cavalli V (2022) Analysis of neuronal injury transcriptional response identifies CTCF and YY1 as co-operating factors regulating axon regeneration. *Front Mol Neurosci* 15:967472.
- Bosanac T, et al. (2021) Pharmacological SARM1 inhibition protects axon structure and function in paclitaxel-induced peripheral neuropathy. *Brain* 144:3226–3238.
- Bratkowski M, et al. (2020) Structural and mechanistic regulation of the pro-degenerative NAD hydrolase SARM1. *Cell Rep* 32:107999.
- Bratkowski M, et al. (2022) Uncompetitive, adduct-forming SARM1 inhibitors are neuroprotective in preclinical models of nerve injury and disease. *Neuron* 110:3711–3726.e16.
- Budayeva HG, Ma TP, Wang S, Choi M, Rose CM (Preprint). Increasing the throughput and reproducibility of activity-based proteome profiling studies with hyperplexing and intelligent data acquisition. *bioRxiv* 2023.09.13.557589.
- Byrnes AE, et al. (2024) A fluorescent splice-switching mouse model enables high-throughput, sensitive quantification of antisense oligonucleotide delivery and activity. *Cell Rep Methods* 4:100673.
- Casey JR, Grinstein S, Orłowski J (2010) Sensors and regulators of intracellular pH. *Nat Rev Mol Cell Biol* 11:50–61.
- Chan K, Truong D, Shangari N, O'Brien PJ (2005) Drug-induced mitochondrial toxicity. *Expert Opin Drug Metab Toxicol* 1:655–669.
- Coleman MP, Höke A (2020) Programmed axon degeneration: from mouse to mechanism to medicine. *Nat Rev Neurosci* 21:183–196.
- Dadon-Nachum M, Melamed E, Offen D (2011) The “dying-back” phenomenon of motor neurons in ALS. *J Mol Neurosci* 43:470–477.
- Doran CG, Sugisawa R, Carty M, Roche F, Fergus C, Hokamp K, Kelly VP, Bowie AG (2021) CRISPR/Cas9-mediated SARM1 knock-out and epitope-tagged mice reveal that SARM1 does not regulate nuclear transcription, but is expressed in macrophages. *J Biol Chem* 297:101417.
- Erickson BK, Mintseris J, Schweppe DK, Navarrete-Perea J, Erickson AR, Nusinow DP, Paulo JA, Gygi SP (2019) Active instrument engagement combined with a real-time database search for improved performance of sample multiplexing workflows. *J Proteome Res* 18:1299–1306.
- Essuman K, Summers DW, Sasaki Y, Mao X, DiAntonio A, Milbrandt J (2017) The SARM1 toll/interleukin-1 receptor domain possesses intrinsic NAD⁺ cleavage activity that promotes pathological axonal degeneration. *Neuron* 93:1334–1343.e5.
- Farley MM, Watkins TA (2018) Intrinsic neuronal stress response pathways in injury and disease. *Annu Rev Pathol* 13:93–116.
- Figley MD, et al. (2021) SARM1 is a metabolic sensor activated by an increased NMN/NAD⁺ ratio to trigger axon degeneration. *Neuron* 109:1118–1136.e11.
- Gerdts J, Summers DW, Sasaki Y, DiAntonio A, Milbrandt J (2013) Sarm1-mediated axon degeneration requires both SAM and TIR interactions. *J Neurosci* 33:13569–13580.
- Gerdts J, Brace EJ, Sasaki Y, DiAntonio A, Milbrandt J (2015) SARM1 activation triggers axon degeneration locally via NAD⁺ destruction. *Science* 348:453–457.
- Gilley J, Coleman MP (2010) Endogenous Nmnat2 is an essential survival factor for maintenance of healthy axons. *PLoS Biol* 8:e1000300.
- Guse AH (2004) Regulation of calcium signaling by the second messenger cyclic adenosine diphosphoribose (cADPR). *Curr Mol Med* 4:239–248.
- Huang K, Zhu WJ, Li WH, Lee HC, Zhao YJ, Lee CS (2023) Base-exchange enabling the visualization of SARM1 activities in sciatic nerve-injured mice. *ACS Sens* 8:767–773.
- Huang T, Choi M, Tzouros M, Golling S, Pandya NJ, Banfai B, Dunkley T, Vitek O (2020) MSstatsTMT: statistical detection of differentially abundant proteins in experiments with isobaric labeling and multiple mixtures. *Mol Cell Proteomics* 19:1706–1723.
- Hughes RO, Bosanac T, Mao X, Engber TM, DiAntonio A, Milbrandt J, Devraj R, Krauss R (2021) Small molecule SARM1 inhibitors recapitulate the SARM1^{-/-} phenotype and allow recovery of a metastable pool of axons fated to degenerate. *Cell Rep* 34:108588.
- Jiang Y, Liu T, Lee CH, Chang Q, Yang J, Zhang Z (2020) The NAD⁺-mediated self-inhibition mechanism of pro-neurodegenerative SARM1. *Nature* 588:658–663.

- Jin Y, Zheng B (2019) Multitasking: dual leucine zipper-bearing kinases in neuronal development and stress management. *Annu Rev Cell Dev Biol* 35:501–521.
- Kim EK, Choi EJ (2015) Compromised MAPK signaling in human diseases: an update. *Arch Toxicol* 89:867–882.
- Kim Y, Zhou P, Qian L, Chuang JZ, Lee J, Li C, Iadecola C, Nathan C, Ding A (2007) MyD88-5 links mitochondria, microtubules, and JNK3 in neurons and regulates neuronal survival. *J Exp Med* 204:2063–2074.
- Ko KW, Devault L, Sasaki Y, Milbrandt J, DiAntonio A (2021) Live imaging reveals the cellular events downstream of SARM1 activation. *Elife* 10:e71148.
- Li WH, et al. (2021) Permeant fluorescent probes visualize the activation of SARM1 and uncover an anti-neurodegenerative drug candidate. *Elife* 10:e67381.
- Li Y, et al. (2022) Sarm1 activation produces cADPR to increase intra-axonal Ca⁺⁺ and promote axon degeneration in PIPN. *J Cell Biol* 221:e202106080.
- Loreto A, et al. (2020) Mitochondrial impairment activates the Wallerian pathway through depletion of NMNAT2 leading to SARM1-dependent axon degeneration. *Neurobiol Dis* 134:104678.
- Loreto A, et al. (2021) Neurotoxin-mediated potent activation of the axon degeneration regulator SARM1. *Elife* 10:e72823.
- Loring HS, Thompson PR (2020) Emergence of SARM1 as a potential therapeutic target for Wallerian-type diseases. *Cell Chem Biol* 27:1–13.
- Loring HS, Ico JD, Nemmara VV, Thompson PR (2020) Initial kinetic characterization of sterile alpha and toll/interleukin receptor motif-containing protein 1. *Biochemistry* 59:933–942.
- Miller BR, Press C, Daniels RW, Sasaki Y, Milbrandt J, DiAntonio A (2009) A dual leucine kinase-dependent axon self-destruction program promotes Wallerian degeneration. *Nat Neurosci* 12:387–389.
- Miyamoto T, et al. (2024) SARM1 is responsible for calpain-dependent dendrite degeneration in mouse hippocampal neurons. *J Biol Chem* 300:105630.
- Moujalied D, Strasser A, Liddell JR (2021) Molecular mechanisms of cell death in neurological diseases. *Cell Death Differ* 28:2029–2044.
- Okada Y, Numata T, Sabirov RZ, Kashio M, Merzlyak PG, Sato-Numata K (2023) Cell death induction and protection by activation of ubiquitously expressed anion/cation channels. Part 3: the roles and properties of TRPM2 and TRPM7. *Front Cell Dev Biol* 11:1246955.
- Osterloh JM, et al. (2012) dSarm/Sarm1 is required for activation of an injury-induced axon death pathway. *Science* 337:481–484.
- Panneerselvam P, Singh LP, Ho B, Chen J, Ding JL (2012) Targeting of proapoptotic TLR adaptor SARM to mitochondria: definition of the critical region and residues in the signal sequence. *Biochem J* 442:263–271.
- Pemberton JM, Pogmore JP, Andrews DW (2021) Neuronal cell life, death, and axonal degeneration as regulated by the BCL-2 family proteins. *Cell Death Differ* 28:108–122.
- Rappsilber J, Mann M, Ishihama Y (2007) Protocol for micro-purification, enrichment, pre-fractionation and storage of peptides for proteomics using StageTips. *Nat Protoc* 2:1896–1906.
- Sagathia V, Patel C, Beladiya J, Patel S, Sheth D, Shah G (2023) Tankyrase: a promising therapeutic target with pleiotropic action. *Naunyn Schmiedebergs Arch Pharmacol* 396:3363–3374.
- Sasaki Y, Engber TM, Hughes RO, Figley MD, Wu T, Bosanac T, Devraj R, Milbrandt J, Krauss R, DiAntonio A (2020) cADPR is a gene dosage-sensitive biomarker of SARM1 activity in healthy, compromised, and degenerating axons. *Exp Neurol* 329:113252.
- Schweppe DK, Eng JK, Yu Q, Bailey D, Rad R, Navarrete-Perea J, Huttlin EL, Erickson BK, Paulo JA, Full-Featured GS (2020) Real-time database searching platform enables fast and accurate multiplexed quantitative proteomics. *J Proteome Res* 19:2026–2034.
- Shan X, et al. (Submitted) Fully defined NGN2 neuron protocol reveals diverse signatures of neuronal maturation. *Cell Rep Methods*.
- Shin JE, Geisler S, DiAntonio A (2014) Dynamic regulation of SCG10 in regenerating axons after injury. *Exp Neurol* 252:1–11.
- Siu M, Sengupta Ghosh A, Lewcock JW (2018) Dual leucine zipper kinase inhibitors for the treatment of neurodegeneration. *J Med Chem* 61:8078–8087.
- Sporny M, et al. (2020) Structural basis for SARM1 inhibition and activation under energetic stress. *Elife* 9:e62021.
- Summers DW, DiAntonio A, Milbrandt J (2014) Mitochondrial dysfunction induces Sarm1-dependent cell death in sensory neurons. *J Neurosci* 34:9338–9350.
- Tang T, et al. (2010) A mouse knock-out library for secreted and transmembrane proteins. *Nat Biotechnol* 28:749–755.
- Tedeschi A, Bradke F (2013) The DLK signalling pathway—a double-edged sword in neural development and regeneration. *EMBO Rep* 14:605–614.
- Tortosa E, Sengupta Ghosh A, Li Q, Wong WR, Hinkle T, Sandoval W, Rose CM, Hoogenraad CC (2022) Stress-induced vesicular assemblies of dual leucine zipper kinase are signaling hubs involved in kinase activation and neurodegeneration. *EMBO J* 41:e110155.
- Uccellini MB, Bardina SV, Sánchez-Aparicio MT, White KM, Hou YJ, Lim JK, García-Sastre A (2020) Passenger mutations confound phenotypes of SARM1-deficient mice. *Cell Rep* 31:107498.
- Watkins TA, Wang B, Huntwork-Rodriguez S, Yang J, Jiang Z, Eastham-Anderson J, Modrusan Z, Kaminker JS, Tessier-Lavigne M, Lewcock JW (2013) DLK initiates a transcriptional program that couples apoptotic and regenerative responses to axonal injury. *Proc Natl Acad Sci U S A* 110:4039–4044.
- Yamazaki Y, Schönherr C, Varshney GK, Dogru M, Hallberg B, Palmer RH (2013) Goliath family E3 ligases regulate the recycling endosome pathway via VAMP3 ubiquitylation. *EMBO J* 32:524–537.
- Zhao ZY, et al. (2019) A cell-permeant mimetic of NMN activates SARM1 to produce cyclic ADP-ribose and induce non-apoptotic cell death. *iScience* 15:452–466.